

The large-scale structure supplies the formation of gas-star misaligned galaxies

MIN BAO ^{1,2} YANMEI CHEN ^{1,2} QIUSHENG GU ^{1,2} HUIYUAN WANG ^{3,4} YONG SHI ^{1,2} AND PENG WANG ⁵

¹*School of Astronomy and Space Science, Nanjing University, Nanjing 210023, China*

²*Key Laboratory of Modern Astronomy and Astrophysics (Nanjing University), Ministry of Education, Nanjing 210023, China*

³*Department of Astronomy, University of Science and Technology of China, Hefei 230026, China*

⁴*Key Laboratory for Research in Galaxies and Cosmology, University of Science and Technology of China, Hefei 230026, China*

⁵*Shanghai Astronomical Observatory, Chinese Academy of Sciences, Nandan Road 80, Shanghai 200030, China*

ABSTRACT

Using the integral field unit data from the Mapping Nearby Galaxies at Apache Point Observatory (MaNGA) survey, we build a sample of gas-star misaligned galaxies. The large-scale environment of misaligned galaxies is dominated by filaments and clusters, while is less dense relative to the gas-star aligned control galaxies. The direction of the large-scale structure (LSS) is defined by its minor axis (\vec{e}_3), which indicates the slowest collapsing direction. For the aligned controls, the gas and stellar spins are preferentially perpendicular to \vec{e}_3 , since these galaxies reside in high-mass host haloes. For the misaligned galaxies, the gas spins also tend to be perpendicular to \vec{e}_3 , suggesting that misaligned gas is recently accreted from the LSS. Meanwhile, there is no correlation between their stellar spins and \vec{e}_3 . There are two possible explanations for this observational phenomenon: (1) the large-scale environments of misaligned galaxies evolve as they grow, with stellar angular momenta acquiring in different environments having different orientations; (2) the correlation between stellar spins and the LSS is smeared out since a relatively higher portion of misaligned galaxies in sheet environments are statistically analysed together with those in filament environments.

Keywords: galaxies: kinematics and dynamics — galaxies: evolution

1. INTRODUCTION

Over the past decades, numerical simulations and large redshift surveys have highlighted the large-scale structure (LSS) in the Universe (Bond et al. 1996; Somerville & Davé 2015). From low to high density, the LSS can be classified into voids, sheets, filaments and clusters. Voids are surrounded by sheets, filaments are at the intersection of sheets, and clusters are at two ends of filaments (Hahn et al. 2007). Large-scale cosmic flows are driven by the buildup of the LSS, with matter migrating from low-density regions to high-density regions (Codis et al. 2012). Around each position in the LSS, the direction of cosmic flow can be described by three orthogonal axes. The major axis represents the direction of the fastest collapse, the minor axis represents the direction of the slowest collapse, and the intermediate axis has a collapse speed between them (Zel'dovich 1970). Therefore, the convergence and divergence of cosmic flows along three axes can indicate the density. For a void, the cosmic flows are divergent along all the axes. For a sheet, the cosmic flow along the major axis is convergent, while the flows along the other two axes are divergent. For a filament, the cosmic flows are convergent along the major and intermediate axes, while divergent along the minor axis. For a cluster, the cosmic flows along all the axes are convergent (Wang et al. 2012).

In the current cold dark matter cosmogony, the assembly of dark matter haloes occurs with the buildup of the LSS. Numerical simulations have revealed the correlation between halo spins and the minor axis of LSS (S_h -LSS correlation), and the dependence of S_h -LSS correlation on halo mass (e.g. Zhang et al. 2009; Wang et al. 2011; Libeskind et al. 2013; Aragon-Calvo & Yang 2014; Forero-Romero et al. 2014; Laigle et al. 2015; Ganeshiah Veena et al. 2018). The

spins of low-mass haloes tend to be parallel with the minor axis of LSS, while the spins of high-mass haloes tend to be perpendicular to the minor axis of LSS. Different numerical simulations gave different critical mass (ranging from $M_h \sim 5 \times 10^{11} h^{-1} M_\odot$ to $M_h \sim 5 \times 10^{12} h^{-1} M_\odot$), at which the S_h -LSS correlation changes from parallel to perpendicular orientation. Voids can be regarded as regions devoid of haloes, sheets typically host the low-mass haloes, while the high-mass haloes primarily reside in filaments and clusters (Cautun et al. 2014). Based on this picture, the transition of parallel to perpendicular S_h -LSS correlations can be explained by the following scenarios (Wang & Kang 2017, 2018). On the one hand, the majority of mass assembly of low-mass haloes occurs within sheets, where the matter migrations are perpendicular to the filaments at their intersection (Figure 12 of Codis et al. 2015). As a result, the low-mass haloes acquire angular momentum parallel with the filaments, which can convert into spins parallel with the minor axis of LSS. On the other hand, mass assembly of high-mass haloes primarily occurs in filaments (including clusters), where the matter migrations are along the filaments (Figure 12 of Codis et al. 2015). The high-mass haloes obtain angular momentum perpendicular to the filaments, ultimately converting into spins perpendicular to the minor axis of LSS.

Galaxies reside in dark matter haloes, and their formation is connected to the assembly of haloes in which they form (Wechsler & Tinker 2018). Hence, we expect that similar correlations also exist between galaxy spins and the minor axis of LSS (S_g -LSS correlation). Using the state-of-the-art hydrodynamic simulation Illustris-1, Wang et al. (2018) investigated the S_g -LSS correlation in the local Universe. The spins of low-mass galaxies are preferentially parallel with the minor axis of LSS, while the spins of high-mass galaxies tend to be perpendicular to the minor axis of LSS, in consistent with the behavior of haloes. Zhang et al. (2015) targeted the Sloan Digital Sky Survey (SDSS) galaxies with host halo mass higher than $10^{11.5} h^{-1} M_\odot$, and found perpendicular S_g -LSS correlations. In addition, Barsanti et al. (2022) studied the S_g -LSS correlation as functions of various galaxy properties for Sydney-AAO Multi-object Integral Field Spectrograph survey (SAMi), and discovered that bulge mass is the dominated parameter in the transition of parallel to perpendicular S_g -LSS correlations. Except bulge mass, other parameters, such as stellar mass, visual morphology, kinematic feature, stellar age, star formation activity and local environment, can also affect the S_g -LSS correlation, which were subsequently confirmed by later studies (Kraljic et al. 2021; Barsanti et al. 2023; Zhang et al. 2015). The bulge components can be proper tracers of galaxy mergers, which primarily happen along the filaments and contribute to perpendicular S_g -LSS correlation.

Kinematically misaligned galaxies are defined as hosting two components (gas and/or stars), which spin in obviously different directions. The misalignments can exist between gas-gas, gas-star and star-star (Corsini 2014). The gas-star misalignment is most universal among the three types, which stands 20-50% in the quiescent galaxies (Sarzi et al. 2006; Davis et al. 2011a; Barrera-Ballesteros et al. 2014), and 2-5% in the star-forming galaxies (Chen et al. 2016; Bryant et al. 2019). This misalignment is believed to form through external processes, dominated by gas accretion (Wang et al. 2011; L’Huillier et al. 2012; Lagos et al. 2015; Zhou et al. 2022; Xu et al. 2022), which delivers gas with spins misaligned relative to the stellar component. However, it is still an open question whether the misaligned gas is accreted from the LSS or gas-rich satellites. If the accreted gas originates from the LSS, we would expect a correlation between the spins of misaligned gas and the minor axis of LSS. To explore this question, we build a sample of gas-star misaligned galaxies (misaligned galaxies for short) from the MaNGA survey. The MaNGA IFU data and sample selection are introduced in Section 2. We present the large-scale environments of the misaligned galaxies in Section 3, and compare them with gas-star aligned control galaxies (aligned controls for short). In Section 4, we study the S_g -LSS correlations for gas and stellar components, and make comparisons between misaligned galaxies and aligned controls.

2. DATA

The data products applied in this study are obtained from the final data release of the MaNGA survey, which includes 10010 unique galaxies. For each MaNGA galaxy, the global properties, including right ascension (RA), declination (Dec), effective radius (Re) and axial ratio (b/a), are extracted from NASA-Sloan Atlas catalog (NSA, Blanton et al. 2011). The distortion-corrected redshift (z_c) is obtained from Tempel et al. (2014) catalog. The global stellar mass (M_\star) is extracted from MaNGA data reduction pipeline (DRP, Law et al. 2016) catalog. The spatially resolved properties, including gas and stellar velocities, are obtained from MaNGA data analysis pipeline (DAP, Westfall et al. 2019). The sky-subtracted and flux-calibrated 3D spectra are obtained from MaNGA DRP. We stack the spectra within $1.5 Re$, and calculate the global 4000 Å break (D_n4000) as the flux ratio between two narrow bands of 3850-3950 Å and 4000-4100 Å. Moreover, we fit the kinematic position angles of gas (ϕ_{gas}) and stellar (ϕ_\star) velocity fields using the python-based package PAFIT. The position angle is defined as a counterclockwise angle between north and

a line bisecting the velocity field. We only fit the spaxels with H α signal-to-noise ratios (S/N) higher than 3 for gas velocity field, and the spaxels with median spectral S/N higher than 3 for stellar velocity field.

Following the method in Zhou et al. (2022), we build a sample of 496 misaligned galaxies from MaNGA galaxies. We refer readers to Zhou et al. (2022) for more details about the sample selection, and only describe the critical criteria here: (1) exclude ‘lineless’ galaxies with H α S/N lower than 3 for more than 90% spaxels within $1.5 R_e$; (2) select candidates of misaligned galaxies having position angle offset $\Delta\phi \equiv |\phi_{\text{gas}} - \phi_{\star}|$ higher than 30° , with robust position angle measurements (i.e. $\phi_{\text{error}} \leq 20^\circ$); (3) visually inspect the candidates, removing ongoing mergers and galaxy pairs.

The large-scale environment around a galaxy is expected to shape the intrinsic properties of it (Kraljic et al. 2018). In the next section, we will study the S_g -LSS correlation for misaligned galaxies, to figure out the origin of misaligned gas (from the LSS or satellites). The LSS characteristics are extracted from the Galaxy Environment for MaNGA Value Added Catalog (GEMA-VAC), which is complete in the redshift range of $z_c \sim [0.01, 0.12]$. We therefore exclude galaxies that are not within this redshift range, leaving 7394 MaNGA galaxies and 395 misaligned galaxies for the following analysis. In order to explore the large-scale environment of misaligned galaxies, we build a control sample of aligned galaxies for comparison. For each misaligned galaxy, we randomly select five aligned controls with similar stellar mass ($|\Delta \log M_{\star}| < 0.1$), stellar population age ($|\Delta D_n 4000| < 0.05$) and redshift ($|\Delta z| < 0.03$) from MaNGA galaxies.

3. LARGE-SCALE ENVIRONMENT

3.1. Distance to filament spine

We reconstruct the 3D filament LSS using a public code named DisPerSE (Sousbie 2011; Sousbie et al. 2011), which applies a scale-free and parameter-free topological algorithm on the 3D discrete distributions of galaxies. DisPerSE stands for Discrete Persistent Structures Extractor, and is developed for the study of the properties of filament structures in the cosmic web of galaxy distribution over large scales in the Universe. Taking RA, Dec and z_c of SDSS galaxies (Tempel et al. 2014) as input parameters, we run the DisPerSE code with a 3σ persistence threshold, which requires the signals of filament structures at least three times higher than the local noise levels. Figure 1(a) displays an illustration of the reconstructed filaments with Dec $\sim [25^\circ, 30^\circ]$. The grey points show the distributions of SDSS galaxies, and the black profiles represent the projected filament spines.

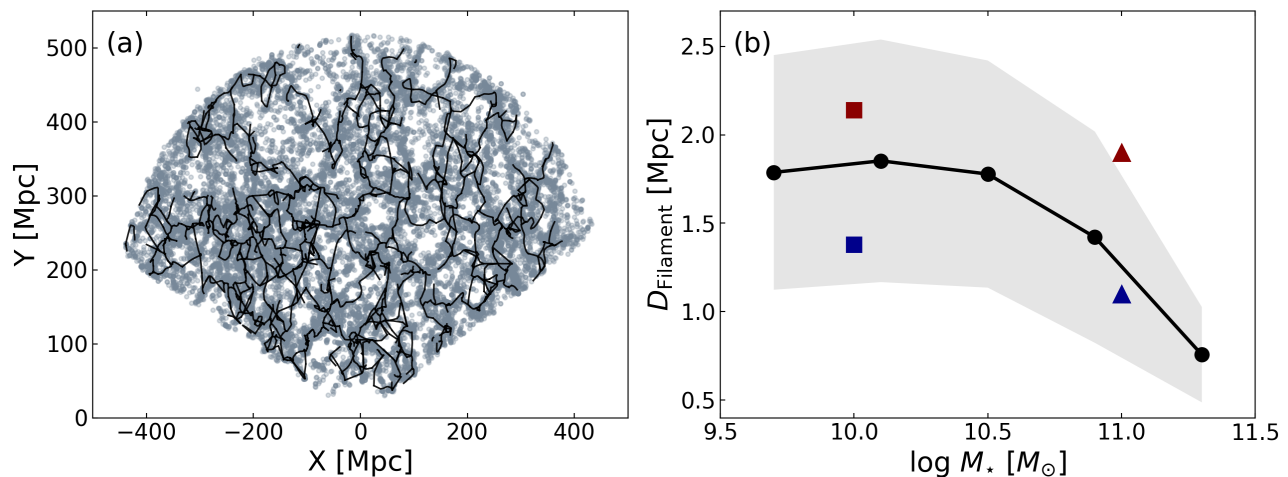


Figure 1. The distances of galaxies to their nearest filament spines in the filament environments. (a) An illustration of the reconstructed filaments with Dec $\sim [25^\circ, 30^\circ]$. The grey points show the distributions of SDSS galaxies. The black profiles represent the projected filament spines. (b) The black solid profile shows the $D_{\text{filament}}-M_{\star}$ correlation for MaNGA galaxies. Each black circle shows the median distance in a certain stellar mass bin. The grey-shaded area shows the 40%-60% scattering region. The red square and triangle show the median D_{filament} for low-mass and high-mass misaligned galaxies, while the blue square and triangle show the median D_{filament} for low-mass and high-mass aligned controls, respectively.

For each MaNGA galaxy, we define D_{filament} as the smallest 3D Euclidian distance from this galaxy to the points in the nearest filament spine (Barsanti et al. 2022). The radii of filaments have been investigated through both observations and simulations (Colberg et al. 2005; Bond et al. 2010; Bonjean et al. 2020; Galárraga-Espinosa et al. 2020; Wang et al. 2021, 2024), which gave typical values spanning from 1 Mpc to 10 Mpc. To explore the correlation between D_{filament} and stellar masses in the filament environments, we only include 4987 galaxies with $D_{\text{filament}} \leq 10$ Mpc from MaNGA galaxies. The black-solid profile in Figure 1(b) displays $D_{\text{filament}}-M_*$ correlation for these galaxies, each black circle shows the median D_{filament} in a certain stellar mass bin. The grey-shaded area shows the 40%-60% scattering region. D_{filament} turns out to decrease with increasing stellar mass, which is consistent with previous studies (Kraljic et al. 2018; Laigle et al. 2018; Welker et al. 2020). We averagely divide the misaligned galaxies and aligned controls with $D_{\text{filament}} \leq 10$ Mpc into low-mass and high-mass subsamples, based on a cutoff of $\log(M_*/M_\odot) = 10.5$. In Figure 1(b), the red square and triangle show the median D_{filament} for low-mass and high-mass misaligned galaxies, while the blue square and triangle show the median D_{filament} for low-mass and high-mass aligned controls. MaNGA galaxies, misaligned galaxies and aligned controls exhibit a consistent trend in the filament environments, where D_{filament} decreases as stellar mass increases. This trend can be explained by a scenario that galaxies migrate towards filament spines as they acquire matter through gas accretion or mergers. Along with the migration, increasing density around a galaxy triggers frequent gas accretion or mergers, supplying the mass assembly of this galaxy. Consequently, galaxies with higher stellar mass tend to locate closer to the filament spines.

3.2. Large-scale environments of misaligned galaxies

Misaligned galaxies are believed to form through external processes, in which their progenitors accrete gas with spins misaligned relative to the stellar component. To figure out the origin of gas accretion (from the LSS or satellites), we make comparisons in large-scale environments between misaligned galaxies and aligned controls. Figure 2(a) displays the normalized distributions of D_{filament} for misaligned galaxies (red) and aligned controls (blue) in the filament environments ($D_{\text{filament}} \leq 10$ Mpc), respectively. The red and blue bars on the top show the corresponding median values of the distances. The misaligned galaxies locate ~ 0.75 Mpc farther away from filament spines than their aligned controls, which implies that these galaxies reside in less dense environments.

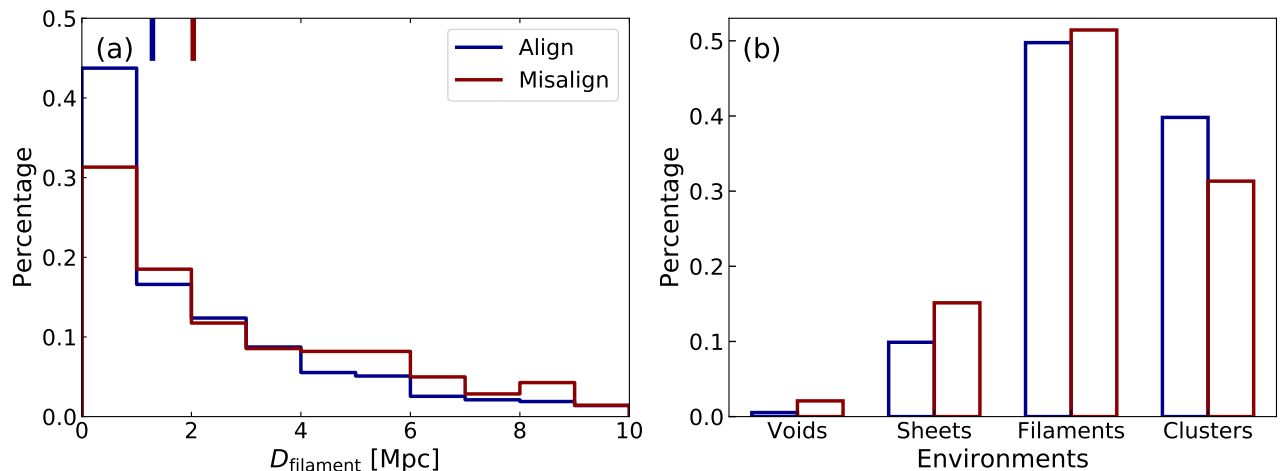


Figure 2. The large-scale environments of misaligned galaxies and their aligned controls. (a) The red histogram displays the distributions of D_{filament} for misaligned galaxies. The blue histogram displays the distributions of D_{filament} for aligned controls. The red and blue bars on the top show the corresponding median distances. (b) The red histograms display the distributions of environments for misaligned galaxies. The blue histograms display the distributions of environments for aligned controls.

To quantify the large-scale environments of misaligned galaxies and aligned controls, we collect the LSS characteristics of these galaxies from the GEMA-VAC catalog. In this catalog, the gravitational potential field is provided by ELUCID project (Exploring the Local Universe with the reConstructed Initial Density field, Wang et al. 2016), which reconstructed the mass density field based on the galaxy groups in the SDSS survey (Yang et al. 2005, 2007). The tidal tensor is the Hessian of the gravitational potential. By diagonalizing the tidal tensor at the position of each

galaxy, three eigenvalues T_1, T_2, T_3 ($T_1 > T_2 > T_3$) can be obtained for this galaxy. The eigenvectors \vec{e}_1, \vec{e}_2 and \vec{e}_3 are computed from corresponding eigenvalues, representing the major, intermediate and minor axes of the LSS. The positive and negative eigenvalues indicate the convergence and divergence of cosmic flows along corresponding axes. Different environments can be classified by three eigenvalues: $T_1, T_2, T_3 < 0$ represents voids; $T_1 > 0$ & $T_2, T_3 < 0$ represent sheets; $T_1, T_2 > 0$ & $T_3 < 0$ represent filaments; $T_1, T_2, T_3 > 0$ represents clusters.

In Figure 2(b), we compare the large-scale environments between misaligned galaxies (red) and aligned controls (blue). On the one hand, the large-scale environments of both misaligned galaxies and aligned controls are dominated by filaments and clusters. On the other hand, more misaligned galaxies reside in voids, sheets and filaments, while less misaligned galaxies reside in clusters compared with their aligned controls. This result is consistent with what we find in Figure 2(a), the misaligned galaxies statistically reside in less dense environments. Such a phenomenon was also reported in the previous studies, e.g. in the ATLAS^{3D} survey (Davis et al. 2011b) and in the MaNGA survey (Jin et al. 2016).

4. FORMATION OF MISALIGNED GALAXIES

Taking advantage of the spatially resolved velocity fields, we compute the spin vectors of gas and stellar components for each MaNGA galaxy following the method in Zhang et al. (2015). Firstly, the inclination angle ζ between the plane of galactic disk and the line of sight is calculated through

$$\sin^2 \zeta = \frac{(b/a)^2 - f^2}{1 - f^2}, \quad (1)$$

where the intrinsic axial ratio (f) is set to 0.14 following Varela et al. (2012). We set $\zeta = 0$ for galaxies with $b/a < f$. Secondly, the spin vector is given by

$$S_x = \cos \alpha \cos \delta \sin \zeta + \cos \zeta (\sin \phi \cos \alpha \sin \delta - \cos \phi \sin \alpha), \quad (2)$$

$$S_y = \sin \alpha \cos \delta \sin \zeta + \cos \zeta (\sin \phi \sin \alpha \sin \delta + \cos \phi \cos \alpha), \quad (3)$$

$$S_z = \sin \delta \sin \zeta - \cos \zeta \sin \phi \cos \delta, \quad (4)$$

where α and δ are RA and Dec, ζ is calculated through Equation (1), and ϕ is taken as ϕ_{gas} and ϕ_{\star} for spin vectors of gas and stellar components, respectively.

To describe the S_g -LSS correlation, we calculate the absolute value of the cosine angle between spin vector and \vec{e}_3 of the LSS at the position of each galaxy, which is given by

$$|\cos \theta| = \frac{|\vec{S} \cdot \vec{e}_3|}{|\vec{S}| \cdot |\vec{e}_3|}, \quad (5)$$

where \vec{S} is the spin vector of gas or stellar component. The gas (or stellar) spin is parallel with \vec{e}_3 when $|\cos \theta| \sim 1$, while the gas (or stellar) spin is perpendicular to \vec{e}_3 when $|\cos \theta| \sim 0$.

Following Zhang et al. (2015), we generate 100 mock samples, each containing the same number of galaxies as the MaNGA sample, to quantify the significance of S_g -LSS correlation for MaNGA galaxies. In each mock sample, \vec{e}_3 directions are kept the same as the relevant MaNGA galaxies, but the spin vectors of the mock galaxies are randomly distributed. The normalized probability distribution function (PDF) of $|\cos \theta|$ is calculated through

$$P(|\cos \theta|) = \frac{N(|\cos \theta|)}{\langle N_m(|\cos \theta|) \rangle}, \quad (6)$$

where $N(|\cos \theta|)$ is the number of MaNGA galaxies in each $|\cos \theta|$ bin, and $\langle N_m(|\cos \theta|) \rangle$ is the average number of mock galaxies in each $|\cos \theta|$ bin among 100 mock samples. We also calculate the normalized standard deviation ($\pm 1\sigma$ scatter) from 100 mock samples as $S(|\cos \theta|) = \sigma_m(|\cos \theta|) / \langle N_m(|\cos \theta|) \rangle$ to assess the significance of correlation, where $\sigma_m(|\cos \theta|)$ is the average standard deviation of $N_m(|\cos \theta|)$ obtained from 100 mock samples. Using a similar method, we calculate the $\pm 2\sigma$ and $\pm 3\sigma$ scatters from 100 mock samples.

Figure 3(a) displays the PDFs of $|\cos \theta|$ for MaNGA galaxies, with green and orange lines representing gas and stellar components, respectively. The green and orange bars on the top of Figure 3(a) mark the median values of $|\cos \theta|$ for gas and stellar components. It turns out that both the gas and stellar spins of MaNGA galaxies tend to

be perpendicular to \vec{e}_3 with $P(|\cos\theta| < 0.5) > 1$. The grey-, blue- and pink-shaded areas in Figure 3(a) show the $\pm 1\sigma$, $\pm 2\sigma$ and $\pm 3\sigma$ scatters from mock samples. It is obvious that the perpendicular signals for both gas and stellar components approach 3σ significance in Figures 3(a). The perpendicular signals arise because these MaNGA galaxies reside in high-mass host haloes. We extract host halo masses for MaNGA galaxies from the Yang et al. (2007) catalog, and found all higher than $M_h \sim 5 \times 10^{11} M_\odot$. The high-mass haloes primarily acquire mass in filaments (including clusters), hence obtain spins perpendicular to the minor axis of the LSS.

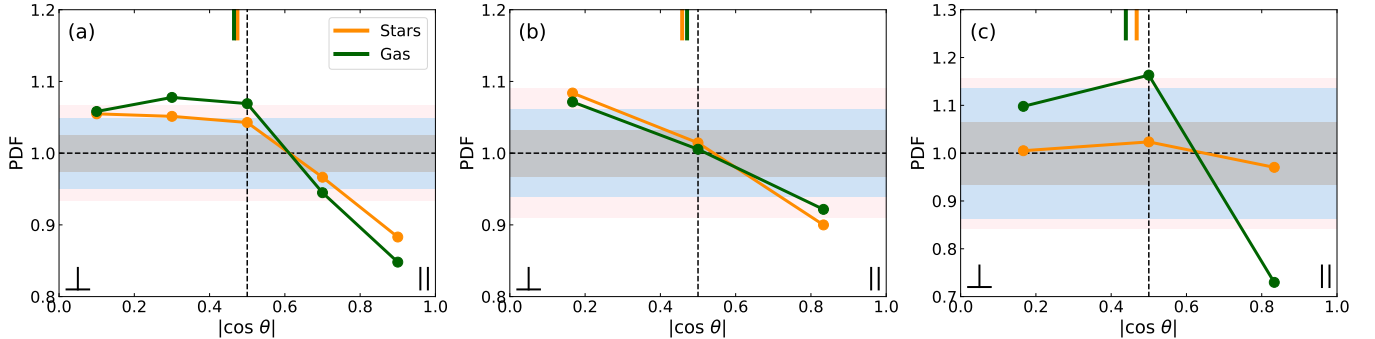


Figure 3. The distributions of $|\cos\theta|$, where θ is the angle between gas (or stellar) spins and \vec{e}_3 of the LSS. (a) The PDFs of $|\cos\theta|$ for MaNGA galaxies. (b) The PDFs of $|\cos\theta|$ for aligned controls. (c) The PDFs of $|\cos\theta|$ for misaligned galaxies. In panels (a), (b) & (c), the green circles show the PDFs of $|\cos\theta|$ between gas spins and \vec{e}_3 , the orange circles show the PDFs of $|\cos\theta|$ between stellar spins and \vec{e}_3 . The green and orange bars on the top mark the corresponding median values. The grey-, blue- and pink-shaded areas show the $\pm 1\sigma$, $\pm 2\sigma$ and $\pm 3\sigma$ scatters for the corresponding mock samples.

Comparing the S_g -LSS correlations between misaligned galaxies and aligned controls can help us in understanding the origin of the accreted gas in the misaligned galaxies. Figure 3(b) displays the normalized PDFs of $|\cos\theta|$ for aligned controls, with green and orange colors representing gas and stellar components. The green and orange bars on the top show the corresponding median values. Both gas and stellar components in the aligned controls show perpendicular signals, approaching 3σ significance (pink-shaded area). Figure 3(c) displays the normalized PDFs of $|\cos\theta|$ for misaligned galaxies, the lines and symbols are color-coded in the same way as that in Figure 3(b). The correlation between gas spins and \vec{e}_3 presents perpendicular signals that approach 2σ significance (blue-shaded area). However, there is no correlation between stellar spins and \vec{e}_3 , as the orange line locates within the grey-shaded area.

Numerical simulations and observational studies (e.g. Wang et al. 2018; Welker et al. 2020; Barsanti et al. 2022) have found evidence of different formation scenarios for low-mass and high-mass galaxies. The majority mass assembly of low-mass galaxies occurs within sheets, hence the galaxy spins are preferentially parallel with the minor axis of LSS. Meanwhile, the mass assembly of high-mass galaxies primarily occurs along filaments, the galaxy spins therefore tend to be perpendicular to the minor axis of LSS. It is within our expectation that the S_g -LSS correlations of gas and stellar components in aligned galaxies (Figure 3b) are consistent with that in MaNGA galaxies (Figure 3a), since the aligned controls are a subset of MaNGA galaxies and reside in high-mass host haloes with $M_h \gtrsim 5 \times 10^{11} M_\odot$. The perpendicular S_g -LSS correlation of gas component in misaligned galaxies agrees with that in aligned controls (Figure 3c), suggesting that misaligned gas is recently accreted from the LSS. It is interesting to find that the stellar spins in misaligned galaxies shows no correlation with the LSS. One possibility is that the large-scale environments of misaligned galaxies evolve as they grow, with stellar angular momenta acquiring in different environments having different orientations. Another possibility is that a higher portion of misaligned galaxies, compared with the aligned controls, reside in sheet environments (Figure 2b). Since these galaxies are statistically analysed together with misaligned galaxies in filament environments, the S_g -LSS correlation of stellar component may be smeared out. To verify these possibilities, we expect to collect data from various IFU surveys, such as SAMI (Croom et al. 2012) and Calar Alto Legacy Integral Field Area (CALIFA) (Sánchez et al. 2012), to enlarge the sample of misaligned galaxies in the future.

5. CONCLUSION

In this study, we build a sample of gas-star misaligned galaxies from the MaNGA survey, as well as an aligned control sample which is closely matched in stellar mass, stellar population age and redshift. We explore the large-scale

environments and the correlations between spins and the large-scale structure for misaligned galaxies and aligned controls to understand the origin of accreted gas in the misaligned galaxies. The main results are as follows:

1. We study the correlation between distances to the nearest filament spines and stellar masses for MaNGA galaxies in the filament environments. The distances turn out to decrease with increasing stellar masses, which favors a scenario of galaxy mass assembly primarily happening with migration towards filament spines. Compared with the aligned controls, the misaligned galaxies locate farther away from filament spines, implying that they reside in less dense environments.
2. From low to high density, the large-scale structure can be classified into voids, sheets, filaments and clusters. The large-scale environments of both misaligned galaxies and aligned controls are dominated by filaments and clusters. Compared with the aligned controls, more misaligned galaxies reside in voids, sheets and filaments, while less misaligned galaxies reside in clusters, which supports the result that misaligned galaxies reside in less dense environments.
3. For the aligned controls, the gas and stellar spins are preferentially perpendicular to the slowest collapsing direction (\vec{e}_3) of the large-scale structure, since these galaxies reside in high-mass host haloes. For the misaligned galaxies, the gas spins also tend to be perpendicular to \vec{e}_3 , suggesting that misaligned gas is recently accreted from the LSS. Meanwhile, there is no correlation between their stellar spins and \vec{e}_3 . One possibility is that the large-scale environments of misaligned galaxies evolve as they grow, with stellar angular momenta acquiring in different environments having different orientations. Another possibility is that the correlation between stellar spins and the LSS is smeared out since a relatively higher portion of misaligned galaxies in sheet environments are statistically analysed together with those in filament environments.

Acknowledgements: MB acknowledges support by the National Natural Science Foundation of China, NSFC Grant No. 12303009. YMC acknowledges support by the National Natural Science Foundation of China, NSFC Grant Nos. 12333002, 11573013, 11733002, 11922302 and the China Manned Space Project, NO. CMS-CSST-2021-A05. HYW acknowledges support by the National Natural Science Foundation of China, Nos. 12192224 and CAS Project for Young Scientists in Basic Research, Grant No. YSBR-062. PW acknowledges support by the NSFC, No. 12473009 and sponsored by Shanghai Rising-Star Program, No.24QA2711100.

Funding for the Sloan Digital Sky Survey IV has been provided by the Alfred P. Sloan Foundation, the U.S. Department of Energy Office of Science, and the Participating Institutions. SDSS- IV acknowledges support and resources from the Center for High-Performance Computing at the University of Utah. The SDSS web site is www.sdss.org. SDSS-IV is managed by the Astrophysical Research Consortium for the Participating Institutions of the SDSS Collaboration including the Brazilian Participation Group, the Carnegie Institution for Science, Carnegie Mellon University, the Chilean Participation Group, the French Participation Group, Harvard-Smithsonian Center for Astrophysics, Instituto de Astrofísica de Canarias, The Johns Hopkins University, Kavli Institute for the Physics and Mathematics of the Universe (IPMU) / University of Tokyo, Lawrence Berkeley National Laboratory, Leibniz Institut für Astrophysik Potsdam (AIP), Max-Planck-Institut für Astronomie (MPIA Heidelberg), Max-Planck-Institut für Astrophysik (MPA Garching), Max-Planck-Institut für Extraterrestrische Physik (MPE), National Astronomical Observatory of China, New Mexico State University, New York University, University of Notre Dame, Observatório Nacional / MCTI, The Ohio State University, Pennsylvania State University, Shanghai Astronomical Observatory, United Kingdom Participation Group, Universidad Nacional Autónoma de México, University of Arizona, University of Colorado Boulder, University of Oxford, University of Portsmouth, University of Utah, University of Virginia, University of Washington, University of Wisconsin, Vanderbilt University, and Yale University.

REFERENCES

- Aragon-Calvo, M. A. & Yang, L. F. 2014, *MNRAS*, 440, L46. doi:10.1093/mnras/slu009
- Barrera-Ballesteros, J. K., Falcón-Barroso, J., García-Lorenzo, B., et al. 2014, *A&A*, 568, A70. doi:10.1051/0004-6361/201423488
- Barsanti, S., Colless, M., Welker, C., et al. 2022, *MNRAS*, 516, 3569. doi:10.1093/mnras/stac2405
- Barsanti, S., Colless, M., D'Eugenio, F., et al. 2023, *MNRAS*, 526, 1613. doi:10.1093/mnras/stad2728

- Blanton, M. R., Kazin, E., Muna, D., et al. 2011, *AJ*, 142, 31. doi:10.1088/0004-6256/142/1/31
- Bond, J. R., Kofman, L., & Pogosyan, D. 1996, *Nature*, 380, 603. doi:10.1038/380603a0
- Bond, N. A., Strauss, M. A., & Cen, R. 2010, *MNRAS*, 409, 156. doi:10.1111/j.1365-2966.2010.17307.x
- Bonjean, V., Aghanim, N., Douspis, M., et al. 2020, *A&A*, 638, A75. doi:10.1051/0004-6361/201937313
- Bryant, J. J., Croom, S. M., van de Sande, J., et al. 2019, *MNRAS*, 483, 458. doi:10.1093/mnras/sty3122
- Cautun, M., van de Weygaert, R., Jones, B. J. T., et al. 2014, *MNRAS*, 441, 2923. doi:10.1093/mnras/stu768
- Chen, Y.-M., Shi, Y., Tremonti, C. A., et al. 2016, *Nature Communications*, 7, 13269. doi:10.1038/ncomms13269
- Codis, S., Pichon, C., Devriendt, J., et al. 2012, *MNRAS*, 427, 3320. doi:10.1111/j.1365-2966.2012.21636.x
- Codis, S., Pichon, C., & Pogosyan, D. 2015, *MNRAS*, 452, 3369. doi:10.1093/mnras/stv1570
- Colberg, J. M., Krughoff, K. S., & Connolly, A. J. 2005, *MNRAS*, 359, 272. doi:10.1111/j.1365-2966.2005.08897.x
- Corsini, E. M. 2014, *Multi-Spin Galaxies*, 486, 51. doi:10.48550/arXiv.1403.1263
- Croom, S. M., Lawrence, J. S., Bland-Hawthorn, J., et al. 2012, *MNRAS*, 421, 872. doi:10.1111/j.1365-2966.2011.20365.x
- Davis, T., Alatalo, K., Bureau, M., et al. 2011, *AAS Meeting Abstracts*
- Davis, T. A., Alatalo, K., Sarzi, M., et al. 2011, *MNRAS*, 417, 882. doi:10.1111/j.1365-2966.2011.19355.x
- Forero-Romero, J. E., Contreras, S., & Padilla, N. 2014, *MNRAS*, 443, 1090. doi:10.1093/mnras/stu1150
- Galárraga-Espinosa, D., Aghanim, N., Langer, M., et al. 2020, *A&A*, 641, A173. doi:10.1051/0004-6361/202037986
- Ganeshaiiah Veena, P., Cautun, M., van de Weygaert, R., et al. 2018, *MNRAS*, 481, 414. doi:10.1093/mnras/sty2270
- Hahn, O., Porciani, C., Carollo, C. M., et al. 2007, *MNRAS*, 375, 489. doi:10.1111/j.1365-2966.2006.11318.x
- Jin, Y., Chen, Y., Shi, Y., et al. 2016, *MNRAS*, 463, 913. doi:10.1093/mnras/stw2055
- Kraljic, K., Arnouts, S., Pichon, C., et al. 2018, *MNRAS*, 474, 547. doi:10.1093/mnras/stx2638
- Kraljic, K., Duckworth, C., Tojeiro, R., et al. 2021, *MNRAS*, 504, 4626. doi:10.1093/mnras/stab1109
- Lagos, C. del P., Padilla, N. D., Davis, T. A., et al. 2015, *MNRAS*, 448, 1271. doi:10.1093/mnras/stu2763
- Laigle, C., Pichon, C., Codis, S., et al. 2015, *MNRAS*, 446, 2744. doi:10.1093/mnras/stu2289
- Laigle, C., Pichon, C., Arnouts, S., et al. 2018, *MNRAS*, 474, 5437. doi:10.1093/mnras/stx3055
- Law, D. R., Cherinka, B., Yan, R., et al. 2016, *AJ*, 152, 83. doi:10.3847/0004-6256/152/4/83
- L’Huillier, B., Combes, F., & Semelin, B. 2012, *A&A*, 544, A68. doi:10.1051/0004-6361/201117924
- Libeskind, N. I., Hoffman, Y., Forero-Romero, J., et al. 2013, *MNRAS*, 428, 2489. doi:10.1093/mnras/sts216
- Sánchez, S. F., Kennicutt, R. C., Gil de Paz, A., et al. 2012, *A&A*, 538, A8. doi:10.1051/0004-6361/201117353
- Sarzi, M., Falcón-Barroso, J., Davies, R. L., et al. 2006, *MNRAS*, 366, 1151. doi:10.1111/j.1365-2966.2005.09839.x
- Somerville, R. S. & Davé, R. 2015, *ARA&A*, 53, 51. doi:10.1146/annurev-astro-082812-140951
- Sousbie, T. 2011, *MNRAS*, 414, 350. doi:10.1111/j.1365-2966.2011.18394.x
- Sousbie, T., Pichon, C., & Kawahara, H. 2011, *MNRAS*, 414, 384. doi:10.1111/j.1365-2966.2011.18395.x
- Tempel, E., Tamm, A., Gramann, M., et al. 2014, *A&A*, 566, A1. doi:10.1051/0004-6361/201423585
- Varela, J., Betancort-Rijo, J., Trujillo, I., et al. 2012, *ApJ*, 744, 82. doi:10.1088/0004-637X/744/2/82
- Wang, J., Navarro, J. F., Frenk, C. S., et al. 2011, *MNRAS*, 413, 1373. doi:10.1111/j.1365-2966.2011.18220.x
- Wang, H., Mo, H. J., Yang, X., et al. 2012, *MNRAS*, 420, 1809. doi:10.1111/j.1365-2966.2011.20174.x
- Wang, H., Mo, H. J., Jing, Y. P., et al. 2011, *MNRAS*, 413, 1973. doi:10.1111/j.1365-2966.2011.18301.x
- Wang, H., Mo, H. J., Yang, X., et al. 2016, *ApJ*, 831, 164. doi:10.3847/0004-637X/831/2/164
- Wang, P. & Kang, X. 2017, *MNRAS*, 468, L123. doi:10.1093/mnrasl/slx038
- Wang, P. & Kang, X. 2018, *MNRAS*, 473, 1562. doi:10.1093/mnras/stx2466
- Wang, P., Guo, Q., Kang, X., et al. 2018, *ApJ*, 866, 138. doi:10.3847/1538-4357/aae20f
- Wang, P., Libeskind, N. I., Tempel, E., et al. 2021, *Nature Astronomy*, 5, 839. doi:10.1038/s41550-021-01380-6
- Wang, W., Wang, P., Guo, H., et al. 2024, *MNRAS*, 532, 4604. doi:10.1093/mnras/stae1801
- Wechsler, R. H. & Tinker, J. L. 2018, *ARA&A*, 56, 435. doi:10.1146/annurev-astro-081817-051756
- Welker, C., Bland-Hawthorn, J., van de Sande, J., et al. 2020, *MNRAS*, 491, 2864. doi:10.1093/mnras/stz2860
- Westfall, K. B., Cappellari, M., Bershady, M. A., et al. 2019, *AJ*, 158, 231. doi:10.3847/1538-3881/ab44a2
- Xu, H., Chen, Y., Shi, Y., et al. 2022, *MNRAS*, 511, 4685. doi:10.1093/mnras/stac354
- Yang, X., Mo, H. J., van den Bosch, F. C., et al. 2005, *MNRAS*, 356, 1293. doi:10.1111/j.1365-2966.2005.08560.x
- Yang, X., Mo, H. J., van den Bosch, F. C., et al. 2007, *ApJ*, 671, 153. doi:10.1086/522027

Zel'dovich, Y. B. 1970, A&A, 5, 84

Zhang, Y., Yang, X., Faltenbacher, A., et al. 2009, ApJ, 706, 747. doi:10.1088/0004-637X/706/1/747

Zhang, Y., Yang, X., Wang, H., et al. 2015, ApJ, 798, 17. doi:10.1088/0004-637X/798/1/17

Zhou, Y., Chen, Y., Shi, Y., et al. 2022, MNRAS, 515, 5081. doi:10.1093/mnras/stac2016